Received: 27 August 2022 | Revised: 4 November 2022 | Accepted: 22 November 2022

DOI: 10.1002/sus2.106

RESEARCH ARTICLE

SusMat WILEY

Elucidating the impact of the ionomer equivalent weight on a platinum group metal-free PEMFC cathode via oxygen limiting current

Hao Wang[1] | **Luigi Osmieri**[1] | **Haoran Yu**[2] | **Michael J. Zachman**[2] | **Jae Hyung Park**[3] | **Nancy N. Kariuki**[3] | **Firat C. Cetinbas**[4] | **Sunilkumar Khandavalli**[1] | **Scott Mauger**[1] | **Deborah J. Myers**[3] | **David A. Cullen**[2] | **Kenneth C. Neyerlin**[1]

[1]Chemistry and Nanoscience Center, National Renewable Energy Laboratory, Golden, Colorado, USA

[2]Center for Nanophase Materials Sciences, Oak Ridge National Laboratory, Oak Ridge, Tennessee, USA

[3]Chemical Sciences and Engineering Division, Argonne National Laboratory, Lemont, Illinois, USA

[4]Nuclear Science and Engineering Division, Argonne National Laboratory, Lemont, Illinois, USA

Correspondence
Luigi Osmieri, MPA-11, Materials Physics and Applications Division, Los Alamos National Laboratory, Los Alamos, NM, 87545, USA.
Email: losmieri@lanl.gov
Kenneth C. Neyerlin, Chemistry and Nanoscience Center, National Renewable Energy Laboratory, Golden, CO 80401, USA.
Email: kenneth.neyerlin@nrel.gov

Abstract

Leveraging the interactions between ionomer and catalyst can increase the performance of proton exchange membrane fuel cells. The impacts of the equivalent weight (EW) of perfluorosulfonic acid–based ionomers on the platinum group metal-free electrode structure and fuel cell performance have not been fully explored. Four membrane electrode assemblies (MEAs) were prepared by using a commercial Fe–N–C catalyst, two perfluorosulfonic acid ionomers with different EWs, that is, Aquivion 720 (A720) and Nafion 1100 (N1100), and two ionomer-to-catalyst (I/C) ratios. The four MEAs were characterized to understand the impact of the ionomer EW and content on the capacitance, proton conductivity, and mass transport on the cathode. The mass transport resistance was measured for the first time using a new oxygen reduction reaction limiting current method enabling to couple the effects of oxygen diffusion with liquid water generation. Low EW ionomer combined with a moderate I/C results in improved performance due to its enhanced proton conductivity. However, when used at high I/C, it can cause severe water flooding at high current density due to the enhanced liquid water uptake, especially at high relative humidity, resulting in lower catalyst utilization and higher mass transport resistance.

KEYWORDS

ionomer equivalent weight, limiting current, mass transport, oxygen reduction reaction, PGM-free catalyst, proton exchange membrane fuel cell

This is an open access article under the terms of the Creative Commons Attribution License, which permits use, distribution and reproduction in any medium, provided the original work is properly cited.
© 2022 The Authors. *SusMat* published by Sichuan University and John Wiley & Sons Australia, Ltd.

26924552, 2023, 1, Downloaded from https://onlinelibrary.wiley.com/doi/10.1002/sus2.106 by National Renewable Energy Lab, Wiley Online Library on [28/02/2023]. See the Terms and Conditions (https://onlinelibrary.wiley.com/terms-and-conditions) on Wiley Online Library for rules of use; OA articles are governed by the applicable Creative Commons License

1 | INTRODUCTION

Proton exchange membrane fuel cells (PEMFCs) are efficient devices for converting the chemical energy in hydrogen to electricity via the electrocatalytic oxidation of hydrogen and reduction of oxygen, with only water and heat as the byproducts.[1–3] As commercially demonstrated since 2015,[4] PEMFCs are viable power sources for electric vehicles with performances comparable to traditional internal combustion engines. However, the performance and efficiency of PEMFCs are still limited by the sluggish kinetics of the cathodic oxygen reduction reaction (ORR), where multiple proton- and electron-transfer processes occur at the gas–liquid–solid interface, thus requiring effective electrocatalysts.[5,6] State-of-the-art ORR catalysts use Pt and its alloys (e.g., PtCo, PtNi),[7] contributing a major portion of the overall PEMFC stack cost and generating a hurdle to widespread implementation for applications such as light-duty vehicles.[8] Therefore, Pt group metal (PGM)-free catalysts using earth-abundant elements are of great interest to improve the cost competitiveness of PEMFCs, with recent advances in ORR activity, fuel cell performance, and most notably, durability of these materials, bringing them closer to viability as replacements for Pt-based cathode catalysts.[9–11] Among the studied PGM-free catalysts, transition metal/nitrogen-doped carbons (M–N–C) represent the state-of-the-art due to their high intrinsic activity, high atomic utilization efficiency, and high electronic conductivity.[12] Ever since the very first M–N–C catalyst developed by Jasinski in 1964,[13] this approach has attracted the attention of many research groups.[14–17] The development of M–N–C catalysts has advanced to the stage where PEMFCs based on these catalysts with reproducible and stable performance are commercially available.[8,18,19]

With decades of efforts on material exploration and electrode fabrication, it became clear that the electrode structure design can play a crucial role in the performance of PEMFCs with PGM-free cathode catalysts. The electrode structure dictates the interactions between the ionomer and catalyst particles. The resulting active site accessibility to both H^+ and O_2 dictates in large part the performance at high current densities necessary for practical applications.[20] Electrode structure optimization is more critical for PGM-free electrodes than for PGM-based electrodes because the lower ORR activity of PGM-free catalysts necessitates much higher loadings to achieve reasonable performances, resulting in ca. 10 times thicker catalyst layers (CLs).[21–23]

Limited yet insightful studies have optimized the catalyst–ionomer ink deposition approach,[24] the catalyst loading,[25,26] the ink dispersing methodology,[27] the ink solvent composition,[28] and the ionomer-to-catalyst ratio (I/C).[29,30] The impact of the ionomer equivalent weight (EW) on the performance of a PEMFC was only investigated with one PGM-free catalyst.[31] However, the EW impact on the electrode structure, such as morphology, ionomer coverage, capacitance, proton conductivity, and mass transfer resistance, has not been studied in detail. Although conventional Nafion ionomers with long side chains have typically been adopted in PEMFCs, they show the limitation of low proton conductivity at low relative humidity (RH), inspiring the development of low EW ionomers with higher levels of crystallinity, thermal resistance, and volumetric density of proton-conducting groups.[32] The ionomer EW is defined as the weight of the dry polymer per ionic group capable of transporting protons (i.e., $-SO_3^-$). In a perfluorosulfonic acid (PFSA)-based ionomer, EW dictates properties, such as proton-exchange capacity, spatial volume, and water uptake.[33] The properties of PFSA are governed not only by the backbone and side chain lengths but also by their chemistry.[34] Therefore, during PEMFC operation, one would expect that ionomers with different EWs will show different interactions with catalyst surfaces and behave differently when exposed to water. This will result in different electrode properties, influencing the PEMFC performance.

Low EW ionomers have attracted great attention due to their shorter H^+ transfer pathway, enabling higher proton conductivity than their higher EW counterparts, as showcased by previous studies of PGM-based PEMFC electrodes.35–37 Even though a strong dependence of the performance on the ionomer EW was not observed in these studies of thin PGM CLs, the ionomer properties are expected to have a greater impact on the performance of thick PGM-free electrodes, calling for further investigation.

Several methods have been established to determine the gas-phase mass transport resistance in a PEMFC CL.[38–40] Our group recently developed a hydrogen oxidation reaction (HOR) limiting current method using a Pt black layer as an integrated sensor to measure the gas mass transport resistance in PGM-free electrodes.[30,41] In this approach, H_2 molecules diffuse through the gas diffusion layer (GDL) and the PGM-free CL (which is electrocatalytically inert to the HOR) to reach the Pt black sensor (PtBS), where they are oxidized. However, the HOR does not generate liquid water, and thus, this sensor configuration does not resemble the actual PEMFC cathode conditions during operation. To address this limitation, in this work we developed an upgraded method to measure the gas transport resistance in the presence of generated liquid water, which is useful for considering the effect of liquid water on the ionomer and on the CL transport properties.

26924552, 2023, 1, Downloaded from https://onlinelibrary.wiley.com/doi/10.1002/sus2.106 by National Renewable Energy Lab, Wiley Online Library on [28/02/2023]. See the Terms and Conditions (https://onlinelibrary.wiley.com/terms-and-conditions) on Wiley Online Library for rules of use; OA articles are governed by the applicable Creative Commons License

Herein, we prepared four different membrane electrode assemblies (MEAs) using a commercial PGM-free Fe–N–C catalyst (from Pajarito Powder LLC) with two different I/C ratios (0.54 and 1.00) and two ionomers with different EW, Aquivion (EW = 720), and Nafion (EW = 1100). The MEAs were characterized electrochemically in a differential cell to examine their polarization behavior, double-layer capacitance, proton-transport resistance, and gas-phase mass transport resistance. We applied our newly developed ORR limiting current method to study O_2 diffusion through the CL in the presence of liquid water generated by the ORR. This new ORR limiting current method was compared with the previous HOR limiting current method. The results indicate that ionomer EW and ionomer content in the CL are key factors affecting PEMFC performance. High density of exchangeable protons and low proton transport resistance are both critical for performance improvement at low current density (kinetic control region of the polarization curve), whereas the effect of the gas transport resistance in the electrode, highly influenced by the ionomer liquid water uptake, is dominant at high current density, where the gas diffusion becomes a limiting factor.

2 | RESULTS AND DISCUSSION

2.1 | Electrode morphology and ionomer distribution within the CCL

To study the impact of the ionomer EW and the ionomer content on the PEMFC performance, two PFSA ionomers with different EWs (A720 and N1100) were used with two I/C ratios (0.54 and 1.00) to prepare the PGM-free catalyst ink (Table S1). The backbone and side chain structure differences between A720 and N1100 are illustrated in Figure S1. Compared to A720, N1100 is a larger molecule with 2.2 more tetrafluoroethylene repeatable units in the backbone (per side chain) and an additional (CF_2CFCF_3) group in the side chain, and therefore fewer exchangeable protons at a given I/C ratio based on the definition of EW (Equation S1). The numbers of exchangeable protons in the four MEAs were calculated based on Equation (S2). The number was the largest for MEA3 (2.78×10^{-5} mol), similar for MEA4 (1.82×10^{-5} mol) and MEA1 (1.50×10^{-5} mol), and the smallest for MEA2 (0.98×10^{-5} mol) as listed in Table S3. The different exchangeable proton values are expected to result in different electrode properties under the operating conditions examined.

In addition to the exchangeable proton number, different ionomer EW and contents gave rise to different electrode structures as visualized by the cross-sectional SEM images (Figure 1B–E). For the electrodes using the same ionomer EW, increasing the I/C ratio from 0.54 to 1.00 leads to greater catalyst aggregates in both size and quantity. Because the ionomer–catalyst interface plays a crucial role in PEMFC performance, F mapping was first carried out at low magnification (5000×) to showcase the ionomer distribution in the CL as shown in Figure 2A, and the resulting F coverage was averaged from three maps for each of the MEAs studied, as summarized in Figure 2B. MEA1 and MEA3 have higher F coverage than the other two MEAs, suggesting that the A720 ionomer distributes more homogeneously compared to N1100.

To obtain insights into the ionomer distribution and the resulting aggregates, rheology experiments were performed on the PGM-free inks with various I/C ratios. The steady-shear rheology results are presented in Figure 2C,D. Without the ionomer (I/C = 0), strong shear thinning was visible, which served as an indication of significant particle agglomeration due to strong van der Waals attraction between the particles. The breakup of the agglomerated structure results in the strong shear thinning response. When the I/C ratio was increased to 0.25, A720 shows Newtonian behavior indicating a significant reduction in agglomeration due to the stabilization of the particles by the ionomer, commonly via a combination of steric hindrance and electrostatic repulsion mechanisms. This observation is consistent with our previous study on PGM-free inks.[43] However, N1100, though reduced compared to 0 I/C, still shear thins at 0.25 I/C, suggesting the existence of some agglomerates (or only partial stabilization of the particles by the ionomer) but approaches Newtonian behavior at a higher I/C of 0.54 suggesting the complete stabilization of the inks. Further increase in I/C, beyond 0.25 and 0.54 for A720 and N1100 inks, respectively, leads to a weak increase in the ink viscosity, suggesting the presence of free/excess ionomer in the bulk that contributes to an increase in their viscosity. Although the differences between A720 and N1100 at I/C ratios of 0.54 and 1.00 become minimal, A720 is slightly more viscous than N1100. This suggest more excess/unbounded A720 molecules in the bulk ink compared to N1100 because a lower amount of this ionomer is required to completely stabilize the particles than N1100. Overall, the low EW ionomer stabilizes the agglomerates more effectively due to the higher charge that provides more electrostatic stabilization to the particles. The comparison of their viscoelasticity, characterized through oscillatory shear rheology measurements (amplitude sweep) at low I/Cs (provided in the Supporting Information section), is also consistent with these steady-shear rheology observations further supporting that the low EW AQ720 ionomer stabilizes the agglomerated structure more effectively compared to the high EW N1100 ionomer.

The USAXS–SAXS data provide the average structural features of the electrode over a wide range of length scales

26924552, 2023, 1, Downloaded from https://onlinelibrary.wiley.com/doi/10.1002/sus2.106 by National Renewable Energy Lab, Wiley Online Library on [28/02/2023]. See the Terms and Conditions (https://onlinelibrary.wiley.com/terms-and-conditions) on Wiley Online Library for rules of use; OA articles are governed by the applicable Creative Commons License

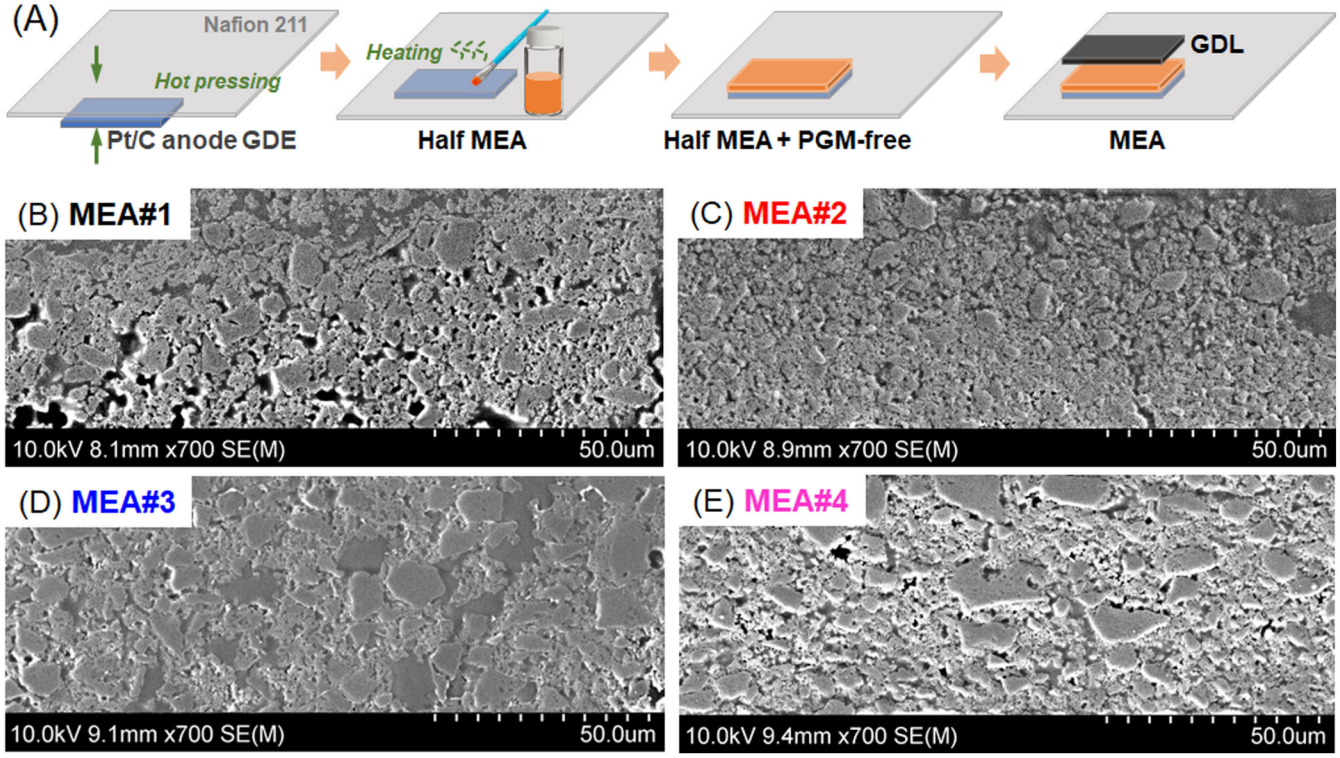

FIGURE 1 (A) Scheme of the membrane electrode assembly (MEA) fabrication process. Cross-sectional SEM images for the cathode catalyst layer (CCL) of (B) MEA1, (C) MEA2, (D) MEA3, and (E) MEA4

from nanometers to several microns, representing the primary catalyst particle size, the catalyst aggregate size, and the catalyst agglomerate size as well as the ionomer agglomerate size. The USAXS–SAXS profiles plotted as scattered intensity ($I(q)$) versus scattering vector (q) for the four MEAs are shown in Figure 2E. The data for the different samples have been offset on the y-axis for the better visualization of the separate curves. Notable features of the scattering profiles are the scattering peak in the 0.008–0.1 $Å^{-1}$ q region for all four electrodes and a slight scattering peak in the 0.0003–0.007 $Å^{-1}$ q region for MEA3 that is absent for the other three electrodes. Figure 2F shows the particle volume distributions determined by fitting the X-ray scattering curves using the Modeling II routine of Irena. These distributions show that the distribution of particles for the four electrodes is nearly identical in the 3–15 nm range but differs in the >15 nm range. The particles in the 3–15 nm range can likely be attributed to either Fe particle embedded in the catalyst, seen as bright spots in the HAADF images. The particles in the 15–20 nm region of the distribution are likely primary carbon particles, and the particles >15 nm are carbon aggregates and agglomerates. Specifically, the MEA3 electrode has a much larger fraction of particles with a mean diameter of ~100 nm. This is in agreement with the SEM data in Figure 1 and TEM EDS data of Figure 2 showing that MEA3 has very large aggregates of carbon compared to the other three samples. The radius of gyration (R_g) of the primary catalyst particles detected by USAXS–SAXS measurements is reported in Table S2, showing a larger radius for the MEAs with a higher I/C ratio and higher EW ionomer.

2.2 | PEMFC polarization curves

The H_2/air polarization curves for the four different MEAs were measured at different RHs (100%, 75%, and 50%) to understand the ionomer EW impact on the PEMFC performance. The results are shown in Figure 3A–C, where the error bars refer to three independent experiments (MEA fabrication and polarization curve measurement) to illustrate the reproducibility. A typical polarization curve can be divided into two main regions: the kinetically-controlled region at low current and the mass transport-controlled region at high current. Figure 3D summarizes the current densities measured at 100% RH at 0.80 and 0.50 V, to represent these two regions, respectively. At 0.80 V, under all the RH conditions examined, MEA3 shows the highest current density, MEA1 and MEA4 show similar values, and MEA2 shows the lowest current density. At 0.50 V at low RHs (75% and 50%), MEA3 still showed the highest current density, and MEA2 showed the lowest. For the other two MEAs, it is worth noting that although MEA4 has a larger number of exchange-

26924552, 2023, 1, Downloaded from https://onlinelibrary.wiley.com/doi/10.1002/sus2.106 by National Renewable Energy Lab, Wiley Online Library on [28/02/2023]. See the Terms and Conditions (https://onlinelibrary.wiley.com/terms-and-conditions) on Wiley Online Library for rules of use; OA articles are governed by the applicable Creative Commons License

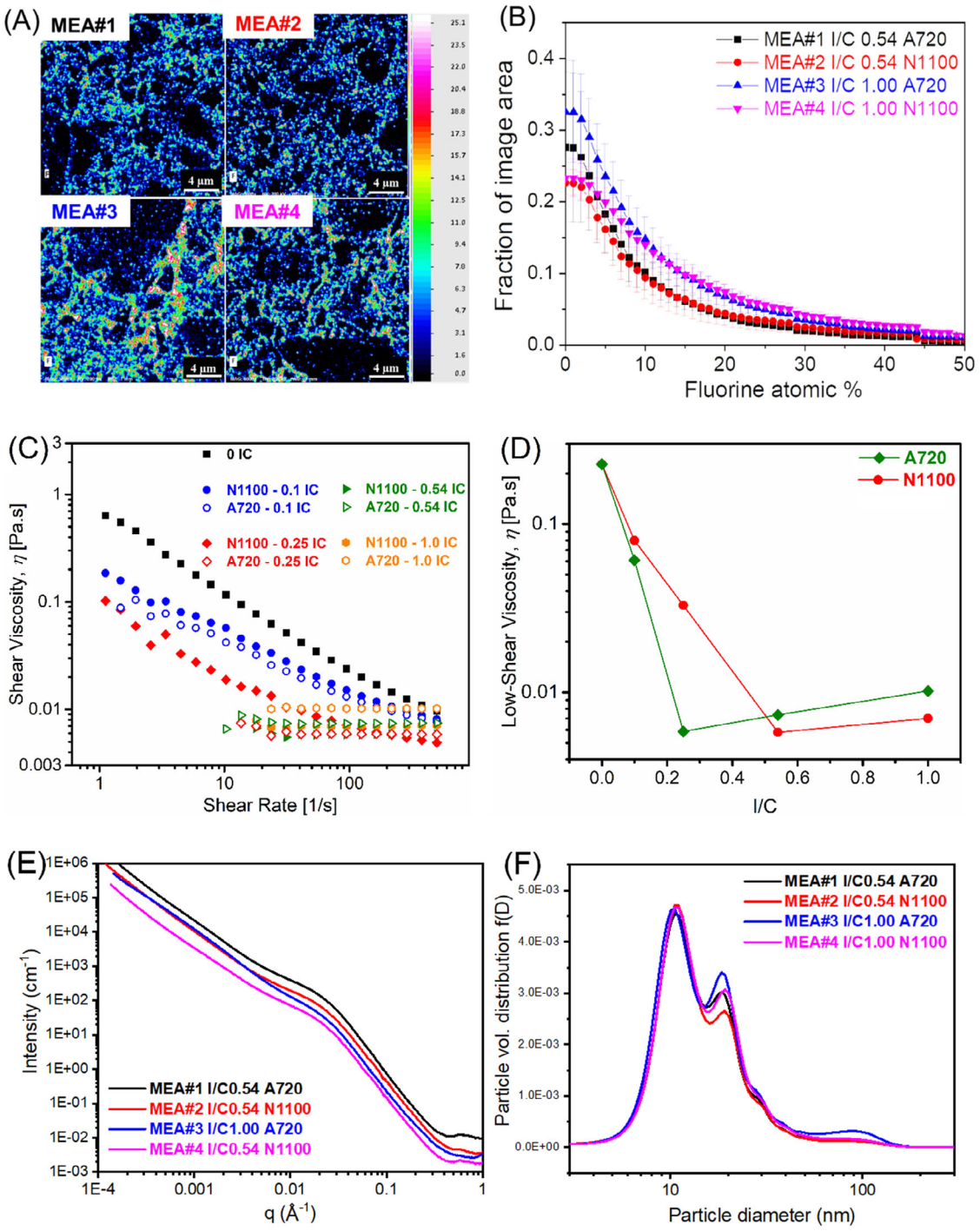

FIGURE 2 (A) F mapping of the four membrane electrode assemblies (MEAs) with the areas chosen from the middle of the catalyst layer (CL) (scale bar: 4 μm); (B) fraction of image area in (A) as a function of fluorine atomic content showing the ionomer coverage; (C) steady-shear viscosity as a function of shear rate to compare different ink compositions; (D) comparison of low-shear viscosity between A720 and N1100 at various ionomer-to-catalyst (I/C) ratios; (E) ultrasmall-angle X-ray scattering–small-angle X-ray scattering (USAXS–SAXS) profiles for cathode electrodes in different equivalent weights (EWs) and ionomer loadings plotted on log–log scales; (F) particle volume distributions derived from fitting the USAXS–SAXS profiles

able protons, it underperformed MEA1. At 0.50 V and 100% RH, MEA3 performed the worst, most likely due to severe water flooding, as indicated by the sharp decrease in voltage in the polarization curve, whereas the other three MEAs kept the same trend. This suggests that the electrode structure is more impactful in the diffusion-controlled region. In fact, at high current densities, MEAs 1 and 2 show the best performances, because they have

26924552, 2023, 1, Downloaded from https://onlinelibrary.wiley.com/doi/10.1002/sus2.106 by National Renewable Energy Lab, Wiley Online Library on [28/02/2023]. See the Terms and Conditions (https://onlinelibrary.wiley.com/terms-and-conditions) on Wiley Online Library for rules of use; OA articles are governed by the applicable Creative Commons License

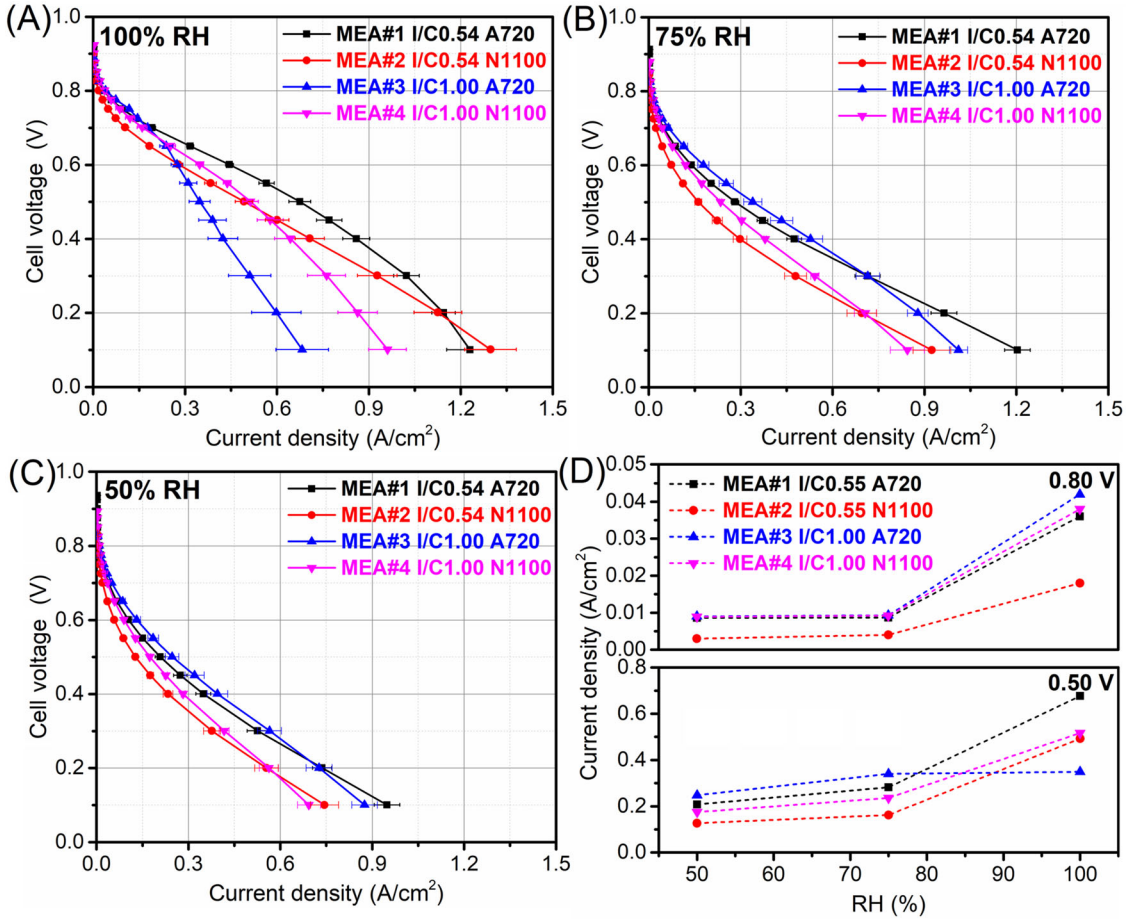

FIGURE 3 H_2/air polarization curves measured at 80°C and 100 kPa gas partial pressure for membrane electrode assemblies (MEAs) fabricated with different ionomer-to-catalyst (I/C) ratios and ionomer equivalent weights (EWs) under (A) 100% relative humidity (RH), (B) 75% RH, and (C) 50% RH; (D) comparison between the current density measured at 100% RH at 0.80 and 0.50 V for the different MEAs

a lower ionomer content, enabling better O_2 diffusion within the CL.[30] because PEMFCs are typically operated at high RH or near saturation,[51] a low EW ionomer with a moderate I/C ratio seems to be the best choice to obtain the highest current densities from this PGM-free catalyst. Similar results were also observed in the H_2/O_2 polarization curves, as shown in Figure 4. The results show consistency with a previously reported study for Pt/C catalysts, that is, the incorporation of an ionomer with short side chain improved PEMFC performance particularly at low RH.[52] Low EW ionomers provide a higher number of exchangeable protons, enabling higher current densities in the kinetic-controlled region. At high current density (diffusion-controlled region), a considerably larger amount of water is generated, causing high mass transfer losses, especially at high RH, as in the case of MEA3. On the other hand, MEA2 with the lowest number of exchangeable protons performed the worst at low RH. However, the exchangeable proton number shows a reverse trend with current density between MEA1 and MEA4, suggesting that there are other factors impacting the performance, which will be discussed in the following sections.

2.3 | Capacitance and proton transfer resistance

Ionomers with different EW values may also impact the electrode capacitance because they represent the interactions between the ionic groups of the PFSA and the accessible catalyst surface. Cyclic voltammetry was measured in H_2/N_2 (anode/cathode gases), where no Faradic processes occurred. The voltammograms under different RHs for each of the studied MEAs are shown in Figure S3, and the comparisons at 100% and 75% RH are shown in Figure 5A,B, respectively. The quasi-rectangular shape of the voltammograms demonstrates characteristic capacitive behavior due to the electrical double-layer charge and discharge for all the MEAs. The redox peaks appearing within the potential range of 0.75–0.80 V are assigned to the Fe^{3+}/Fe^{2+} redox couple from atomically dispersed

26924552, 2023, 1, Downloaded from https://onlinelibrary.wiley.com/doi/10.1002/sus2.106 by National Renewable Energy Lab, Wiley Online Library on [28/02/2023]. See the Terms and Conditions (https://onlinelibrary.wiley.com/terms-and-conditions) on Wiley Online Library for rules of use; OA articles are governed by the applicable Creative Commons License

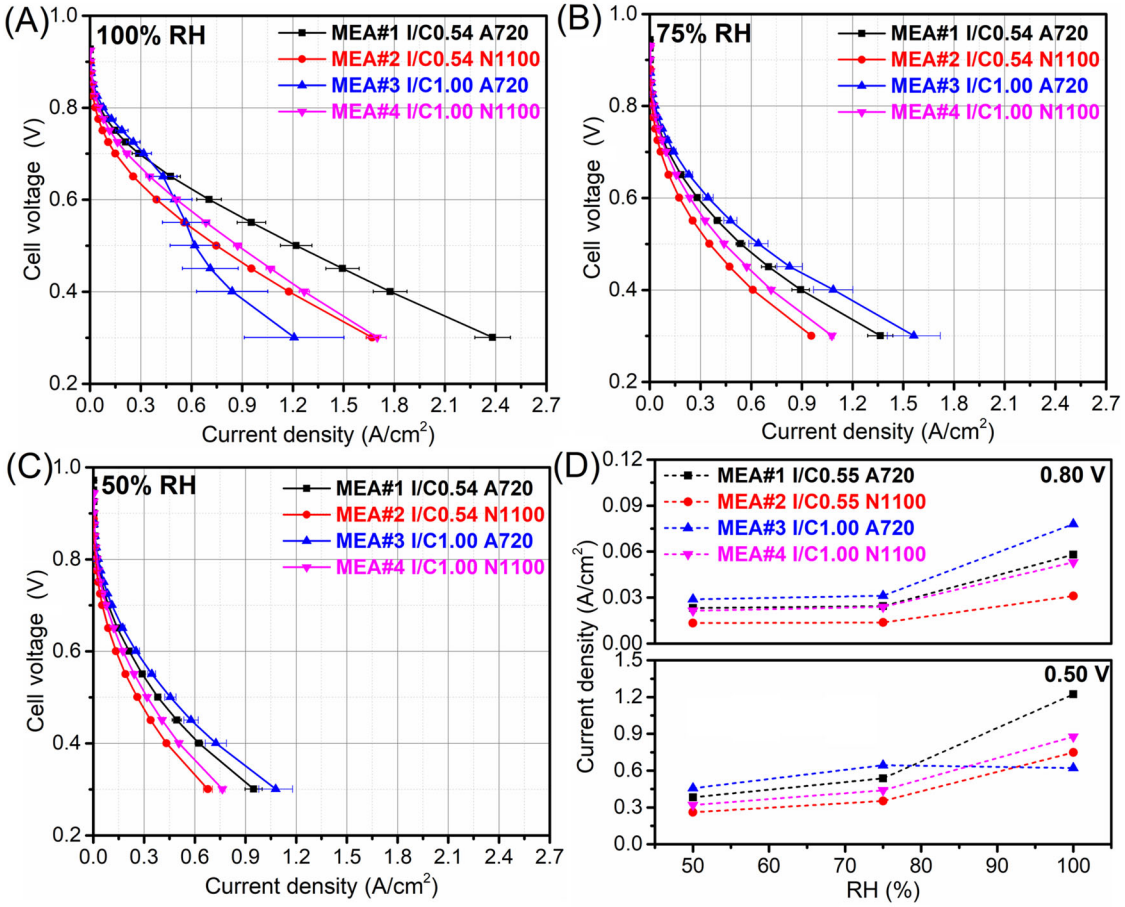

FIGURE 4 H_2/O_2 polarization curves measured at 80°C for membrane electrode assemblies (MEAs) fabricated with different ionomer-to-catalyst (I/C) ratios and ionomer equivalent weights (EWs) under (A) 100% relative humidity (RH), (B) 75% RH, and (C) 50% RH; (D) comparison between the current density measured at 100% RH at 0.80 and 0.50 V for each MEA

Fe–N_x sites.[53,54] The capacitance is proportional to the integrated area of the voltammogram (see Equation S3); the calculated capacitance values are listed in Table S3. Under all RH conditions, the capacitance followed the trend of MEA3 > MEA1 > MEA4 > MEA2, in good agreement with the kinetic current density trend in the polarization curves. This indicates that at a given I/C ratio, a low EW ionomer (providing more exchangeable protons) enables a higher electrochemically active surface area (ECSA) due to better interaction between the catalyst surface and the electrolyte. This observation also agrees well with the rheology and SAXS/USAXS results, confirming that the A720 ionomer had a better interaction with the catalyst surface, presumably due to the higher number of exchangeable protons per unit area of catalyst surface than the N1100 ionomer. Additionally, by comparing MEAs with the same ionomer, increasing the I/C ratio also results in an increase in ECSA. Figure 5C shows the normalized capacitance (C_N) as a function of RH. C_N represents the capacitance at a given RH divided by the capacitance at 100% RH. For the electrodes fabricated with A720, increasing the I/C from 0.54 to 1.00 significantly increased the C_N at all RH values, indicating that introducing more proton-conducting groups into the CL resulted in less of a dependence capacitance on RH. However, for the electrodes with N1100, increasing the I/C ratio did not necessarily result in a C_N increase, demonstrating that an excess of N1100 ionomer leads to ionomer agglomerate between the catalyst particles, rather than uniform coverage of the catalyst surface. This is confirmed by the uneven ionomer distribution in MEA4 observed from the microscopy and F-mapping images.

To understand the impact of the ionomer EW and I/C ratio on the proton transfer resistance within the CL, EIS was performed in H_2/N_2 at various RHs, and the resulting Nyquist plots for each MEA are shown in Figure S4. Parts (D) and (E) of Figure 5 show the comparison of the MEAs at 100% and 75% RH, respectively. The effective proton transfer resistance ($R_{eff}^{H^+}$) in the CLs was calculated from fitting the EIS data with a transmission line model considering planar and spherical diffusion.[55] The software used for the fitting is the Open Source Impedance Fitter (OSIF

26924552, 2023, 1, Downloaded from https://onlinelibrary.wiley.com/doi/10.1002/sus2.106 by National Renewable Energy Lab, Wiley Online Library on [28/02/2023]. See the Terms and Conditions (https://onlinelibrary.wiley.com/terms-and-conditions) on Wiley Online Library for rules of use; OA articles are governed by the applicable Creative Commons License

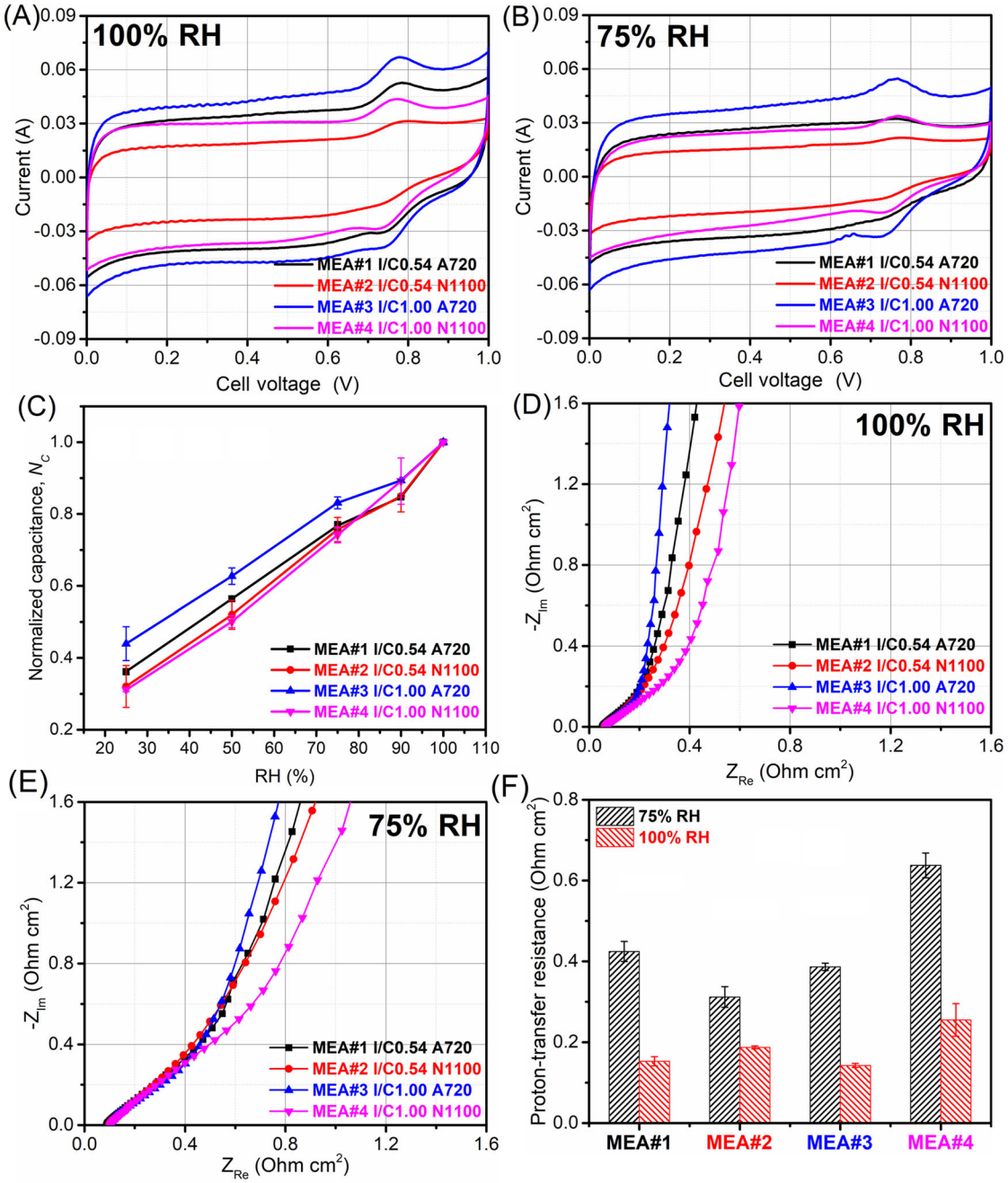

FIGURE 5 Cyclic voltammograms of the cathode catalyst layers (CCLs) of the four membrane electrode assemblies (MEAs) at (A) 100% relative humidity (RH) and (B) 75% RH, and (C) comparison of the normalized capacitance as a function of RH. Nyquist plots of the H_2/N_2 electrochemical impedance spectroscopy of the CCLs at (D) 100% RH and (E) 75% RH, and (F) comparison of the proton-transfer resistance of the CCLs of the four MEAs at different RHs

v2.0).[56] The equivalent circuit used for the fitting is a transmission line circuit model modified with the equations of cylindrical and spherical diffusions.[30,57] The calculated proton transfer resistance comparison at 100% and 75% RH is summarized in Figure 5F. A good match between the experimental and fitted data is shown in Figure S4. At a given RH, all MEAs showed a similar intercept value with the real axis (e.g., ca. 60 mΩ cm^2 at 100% RH). This value is defined as the HFR and represents the sum of the electronic resistance of the electrodes, cables, and cell hardware (current collectors, bipolar plates) plus the ionic resistance of the membrane. The reproducibility of the HFR value across all the MEAs tests indicates that our MEA fabrication and testing procedure is reproducible and does not cause shorting or interfacial contact issues. At 100% RH, MEA3 (the one with the highest number

26924552, 2023, 1, Downloaded from https://onlinelibrary.wiley.com/doi/10.1002/sus2.106 by National Renewable Energy Lab, Wiley Online Library on [28/02/2023]. See the Terms and Conditions (https://onlinelibrary.wiley.com/terms-and-conditions) on Wiley Online Library for rules of use; OA articles are governed by the applicable Creative Commons License

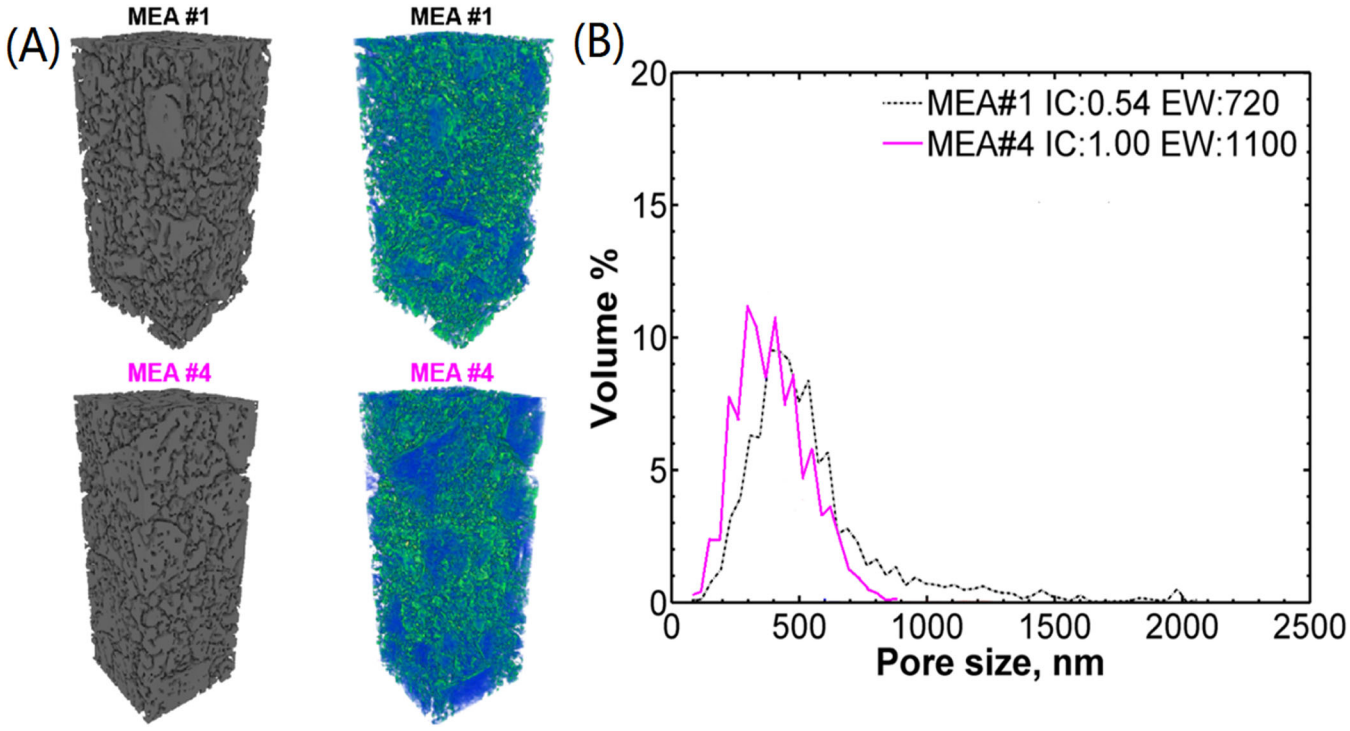

FIGURE 6 (A) Nano-CT segmented phase contrast images and ionomer distribution images (green represents ionomer; blue represents catalyst wall) for the cathode catalyst layer (CCL) of MEA1 and MEA4; (B) pore diameter distribution of the CCLs of MEA1 and MEA4

of exchangeable protons) shows the smallest $R_{\text{eff}}^{H^+}$ value. MEA1 showed a slightly lower $R_{\text{eff}}^{H^+}$ than MEA2 because A720 has a shorter backbone and side chain than N1100 (Figure S1) and consequently provides a shorter protonic transfer pathway within the electrode. However, at 75% RH, MEA2, having a more compact electrode structure than MEA 1 (see Figure 1B,C), showed a lower $R_{\text{eff}}^{H^+}$ due to a less tortuous H^+ conduction path. Among all the MEAs, MEA4 showed the largest $R_{\text{eff}}^{H^+}$, regardless of RH. In comparison with MEA2, increasing the I/C from 0.54 to 1.00 did not facilitate proton transfer. The relatively low capacitance and high proton transfer resistance of MEA4 might be the consequence of its electrode structure with low ionomer coverage between large carbon aggregates, as observed from HAADF and F-mapping images (Figure S2).

2.4 | Nano-CT characterization

To understand why MEA4 showed lower performance and higher proton transfer resistance than MEA1, despite their very similar number of exchangeable protons, we conducted the 3D nano-CT characterization of the CCLs of these two MEAs to visualize their electrode morphology and ionomer distribution. The volume renders of the segmented phase contrast images to show the overall structural morphology of the scanned areas are displayed in Figure 6A. The observations are consistent with the SEM images, suggesting that the CCL of MEA1 has smaller and more uniform carbon aggregates than the CCL of MEA4. The R_g values in Table S2 also confirm these results. The ionomer distribution (green color) images show more uniform and higher coverage over the catalyst surface in MEA1 than in MEA4. MEA4 shows a strong adsorption intensity on the outer surface of large catalyst particles, suggesting a predominant presence of large ionomer agglomerates with poor penetration into the pores in the catalyst aggregates and agglomerates. A few large ionomer agglomerates are also visible next to the catalyst aggregates. MEA1 shows an absorption signal both inside and outside the catalyst particles, suggesting better ionomer penetration inside the pores and/or within smaller catalyst aggregates. These results may explain the higher proton transfer resistance of MEA4: The presence of larger and isolated ionomer agglomerates between the catalyst aggregates results in a more tortuous path for proton mobility within the CCL. The ionomer agglomeration and isolation in MEA4 also gave rise to lower capacitance and higher capacitance dependence on RH than for MEA1. Additionally, MEA1 has larger pores (mean diameter of ca. 500 nm) between the large catalyst aggregates compared to MEA4 (mean diameter of ca. 300 nm) according to the pore size distribution (Figure 6B). This indicates that the CCL in MEA1 is more porous than that in MEA4, facilitating gas-phase mass transport, which will be discussed in detail in the following sections.

26924552, 2023, 1, Downloaded from https://onlinelibrary.wiley.com/doi/10.1002/sus2.106 by National Renewable Energy Lab, Wiley Online Library on [28/02/2023]. See the Terms and Conditions (https://onlinelibrary.wiley.com/terms-and-conditions) on Wiley Online Library for rules of use; OA articles are governed by the applicable Creative Commons License

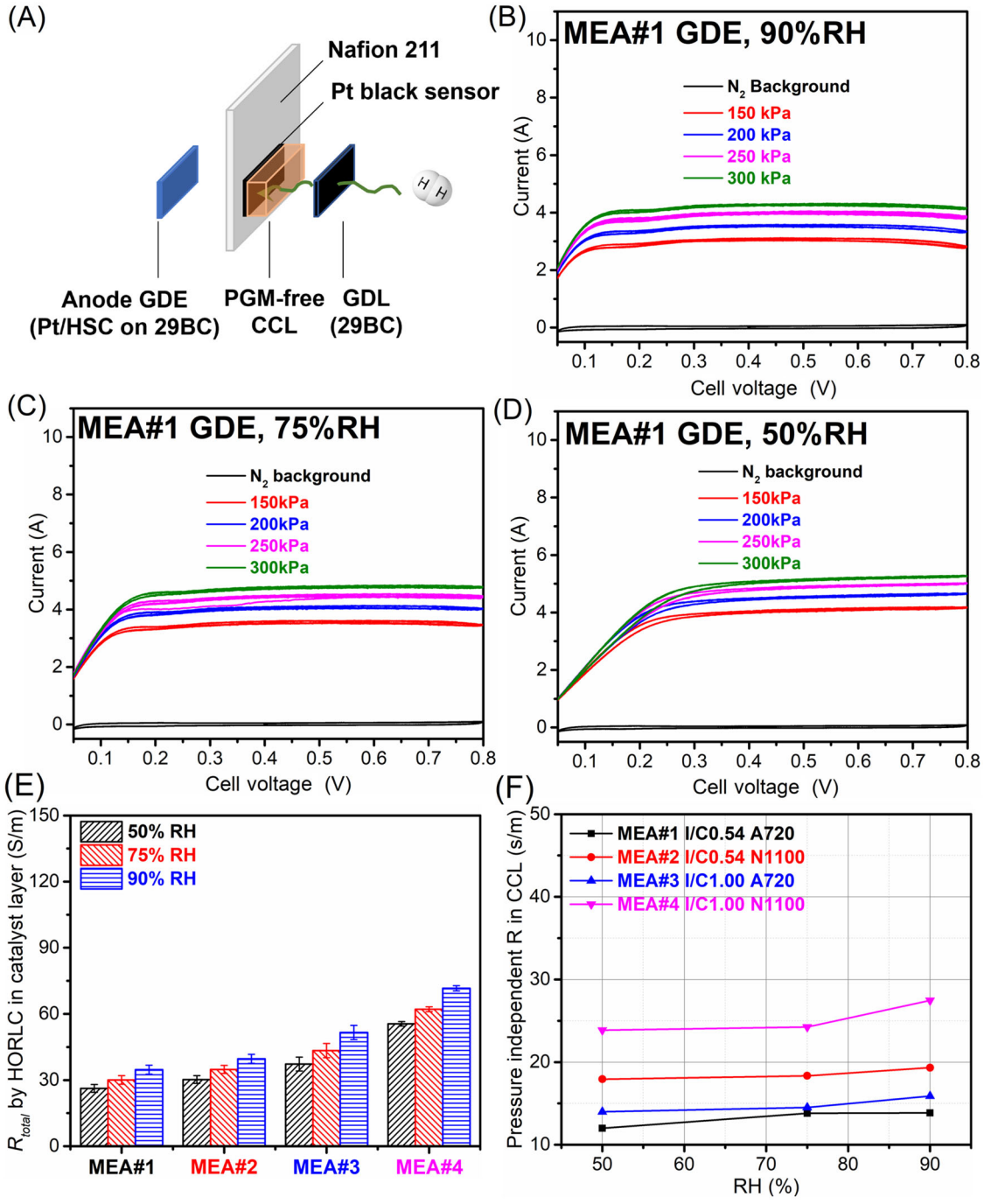

FIGURE 7 (A) Membrane electrode assembly (MEA) configuration of the hydrogen oxidation reaction (HOR) limiting current measurements; cyclic voltammograms of MEA1 cathode gas diffusion electrode (GDE) as an example under different pressures in (B) 90% relative humidity (RH), (C) 75% RH, and (D) 50% RH; (E) total transport resistance (R_{total}) in the cathode catalyst layer (CCL) for the studied MEAs at 150 kPa of gas and water pressure; (F) pressure-independent transport resistance (R_{NP}) as a function of RH

2.5 | Mass transport resistance by an HOR limiting current technique

To investigate the impacts of the ionomer EW and I/C ratio on the bulk gas transport resistance in the CCL, we first used the HOR limiting current technique. Figure 7A shows the MEA configuration, in which the PGM-free CCL was deposited onto the PtBS. Figure 7B–D shows the CVs of MEA1 GDE as an example under different pressures at 90%, 75%, and 50% RH, respectively. First, the CVs were obtained by flowing 5% H_2 (in N_2 balance) and pure N_2 on the anode and cathode, respectively, to obtain

26924552, 2023, 1, Downloaded from https://onlinelibrary.wiley.com/doi/10.1002/sus2.106 by National Renewable Energy Lab, Wiley Online Library on [28/02/2023]. See the Terms and Conditions (https://onlinelibrary.wiley.com/terms-and-conditions) on Wiley Online Library for rules of use; OA articles are governed by the applicable Creative Commons License

background capacitive currents (black lines). Then, CVs were measured by flowing 5% H_2 to both electrodes to obtain actual HOR limiting currents, as in a H_2 pump experiment. According to Figure 7B–D, at fixed RH, the HOR limiting current increases with pressure. It is also observed that the HOR limiting current decreases with the increasing RH if the pressure is kept constant. An RH of 90% was the highest used in this mass transport study because further increasing the RH to 100% caused issues caused by water flooding (Figure S5), where no linearity was found between the current density and pressure. The limiting current, after subtracting the background, can be converted to the total bulk-electrode gas transport resistance in the GDE ($R^{H_2}_{\text{total, GDE}}$) based on Equation (S4). To rule out the contribution of the GDL, an MEA without a PGM-free CL was fabricated as a reference (Figure S6A), and the resulting CVs are shown in Figure S6B–D. Similarly, the limiting current after subtracting the background can be converted into the total bulk-electrode gas transport resistance in the GDL ($R^{H_2}_{\text{total, GDE}}$) based on Equation (S5). Therefore, the total gas transport resistance in the CCL ($R^{H_2}_{\text{total, GDE}}$) was obtained from $R^{H_2}_{\text{total, GDE}}$ after subtracting the $R^{H_2}_{\text{total, GDE}}$ at each pressure and each RH (Equation S6). The same calculation procedure was applied to the four MEAs.

Figure 7E compares the $R^{H_2}_{\text{total, GDE}}$ for all the studied MEAs under different RHs, and the values are summarized in Table S4. These values are indicative of the gas diffusion resistance within CL, without the presence of liquid water generated by the ORR. $R^{H_2}_{\text{total, GDE}}$ follows the trend of MEA4 > MEA3 > MEA2 > MEA1 under all RHs, suggesting that vapor water uptake had little impact on the ionomer spatial distribution and volume in the CCL. At a given I/C ratio, the lower EW ionomer seems to occupy less space in the CCL pores, resulting in a lower gas transport resistance. R_{total} can be broken down into two components, that is, the pressure-dependent resistance (R_P) and the pressure-independent resistance (R_{NP}). The former is the contribution from molecular diffusion in the pores larger than ca. 20 nm, and the latter represents the contribution from Knudsen diffusion through smaller pores in combination with diffusion through ionomer films.[30,41,58] Because this study used the same catalyst but different I/C ratios and different ionomer EWs, the R_{NP} provides a very good indication of the ionomer distribution and occupancy in the CCL. The R_{NP} was calculated as the straight line ordinate intercept by plotting R_{total} as a function of the pressure for each individual RH. Figure 7F shows the R_{NP} as a function of RH for the studied MEAs; the values are summarized in Table S4. Clearly, the MEAs with N1100 show higher R_{NP} than those with A720. This indicates that the ionomer with higher EW distributes less homogeneously within the CL, forming more clusters, thus providing more obstacles for the gas molecular diffusion (higher tortuosity) compared to the ionomer with lower EW. These results are in agreement with the SEM images, the nano-CT data, and the in situ electrochemical diagnostic data. In fact, the data in Figure 5C,F show a higher dependence of C_N on RH and higher proton transfer resistance for the N1100 MEAs than for the A720 MEAs. These are clear indications of a less homogeneous ionomer distribution in the CL and lower catalyst particle coverage. Overall, MEA4 with a high I/C ratio and high ionomer EW showed the highest gas transport resistance by the HOR limiting current technique. These results, together with its higher proton transfer resistance (see Figure 5F), explain MEA4's lower performance compared to MEA1 (see Figures 4 and 5) despite its slightly higher number of exchangeable protons. However, these HOR limiting current results and the current density in the H_2/air polarization curves do not explain why MEA3 showed the worst performance in the diffusion-controlled regions at 100% RH (see Figures 3A and 4A). Overall, the HOR limiting current is a good method to characterize the electrode porous structure in terms of catalyst particle size and ionomer distribution structure. However, this technique does not consider the presence of liquid water in the CCL generated during fuel cell operation. For this reason, a new technique for mass transport resistance measurement in the presence of liquid water generated by the ORR was developed and will be described in the next section.

2.6 | Mass transport resistance by a new ORR limiting current technique

To consider the liquid water generated by the ORR within the CCL and its impact on the gas transport resistance, we herein report a new approach to measure the total bulk-electrode gas transport resistance in the CCL ($R^{O_2}_{\text{total, CCL}}$) based on the ORR limiting current. Figure 8A displays the MEA configuration, in which the PGM-free CCL was deposited on a piece of GDL, and another piece of GDL was placed between the PtBS- and PGM-free CL to interrupt the H^+ transfer pathway, thus preventing the ORR from taking place in the PGM-free CL. In this way, the O_2 diffuses through the whole thickness of the PGM-free CL to reach the PtBS, where the ORR occurs. More specifically, during the ORR limiting current measurements, the diluted O_2 (5% in N_2) diffuses from the flow field, reaches the PtBS through the cathode GDE and the additional GDL, and is reduced into water on the PtBS. The generated liquid water diffuses back into the PGM-free CL, further affecting O_2 diffusion, thus more closely resembling an operating

26924552, 2023, 1, Downloaded from https://onlinelibrary.wiley.com/doi/10.1002/sus2.106 by National Renewable Energy Lab, Wiley Online Library on [28/02/2023]. See the Terms and Conditions (https://onlinelibrary.wiley.com/terms-and-conditions) on Wiley Online Library for rules of use; OA articles are governed by the applicable Creative Commons License

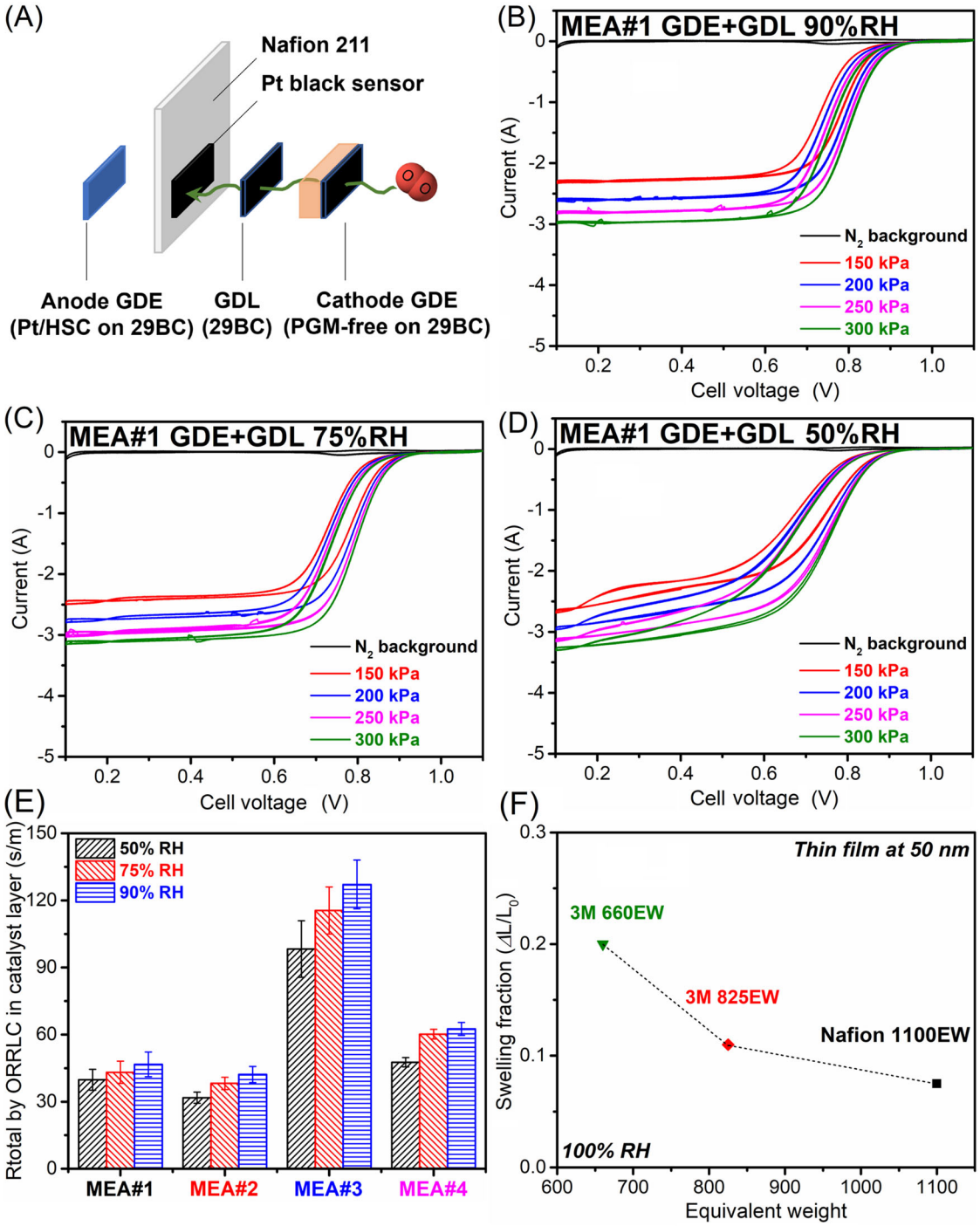

FIGURE 8 (A) Membrane electrode assembly (MEA) configuration of O_2 reduction reaction limiting current measurements for cathode gas diffusion electrode + gas diffusion layer (GDE + GDL); cyclic voltammograms of MEA1 GDE as an example under different pressures in (B) 90% relative humidity (RH), (C) 75% RH, and (D) 50% RH; (E) total transport resistance (R_{total}) in the cathode catalyst layer (CCL) for the studied MEAs at 150 kPa of gas and water pressures; (F) swelling fraction of ionomer thin film at 50 nm as a function of equivalent weight (EW) at 100% RH

PEMFC cathode in terms of gas mass transport within the CCL and ionomer liquid water uptake. By comparing Figures 7A and 8A, it is possible to better understand the substantial differences between the HOR and the ORR limiting current methods. Figure 8B–D shows the CVs of MEA1 cathode GDE + GDL as an example under different pressures in 90%, 75%, and 50% RH, respectively. The CVs were measured while flowing pure H_2 and pure N_2 on the anode and cathode, respectively, to obtain background capacitive currents (black lines). Then the cathode

26924552, 2023, 1, Downloaded from https://onlinelibrary.wiley.com/doi/10.1002/sus2.106 by National Renewable Energy Lab, Wiley Online Library on [28/02/2023]. See the Terms and Conditions (https://onlinelibrary.wiley.com/terms-and-conditions) on Wiley Online Library for rules of use; OA articles are governed by the applicable Creative Commons License

gas was switched to 5% O_2 (in N_2) to obtain the actual ORR limiting currents. According to Figure 8B–D, at fixed RH, the ORR limiting current increases with pressure. It is also observed that the ORR limiting current decreases with increasing RH if the pressure is kept constant. An RH of 90% was the highest used in these measurements because further increasing the RH to 100% also caused severe water flooding (Figure S7), where no linearity can be observed between current density and pressure. The limiting current after subtracting the background can be converted into the total bulk-electrode gas transport resistance in the cathode GDE and the additional GDL ($R^{O_2}_{\text{total, GDE+GDL}}$) based on Equation (S7). To rule out the contribution of the two pieces of GDL, an MEA without a PGM-free CL was fabricated as a reference (Figure S8A), and the resulting CVs are shown in Figure S8B–D. Similarly, the limiting current after subtracting the background can be converted to the total bulk-electrode gas transport resistance in the two pieces of GDL ($R^{O_2}_{\text{total, 2×GDL}}$) based on Equation (S8). Therefore, $R^{H_2}_{total,\ CCL}$ was obtained from $R^{O_2}_{\text{total, GDE+GDL}}$ after subtracting $R^{O_2}_{\text{total, 2×GDL}}$ under each pressure and each RH (Equation S9).

Figure 8E compares $R^{H_2}_{total,\ CCL}$ for all the studied MEAs under different RHs; the values are summarized in Table S5. Unlike the HOR limiting current results, the total O_2 transport resistance follows the trend of MEA3 > MEA4 > MEA1 > MEA2. As mentioned before, with the same I/C ratio, the lower EW ionomer occupies less space within the pores in the CCL, resulting in lower gas transport resistance. Nevertheless, in the ORR limiting current results, we observe a reverse trend, that is, the lower EW ionomer causes higher O_2 gas transport resistance. Although no experimental data were found on A720, Figure 8F adapted from Ref. [33] shows the trend that the swelling of ionomer thin films decreases with increasing ionomer EW. This explains the O_2 gas transport resistance for the four studied MEAs, that is, A720 showed much higher liquid water uptake than N1100 and, therefore, occupied more space in the CCL, giving rise to higher gas transport resistance. Another difference from the HOR limiting current results is that the R_{total} obtained from the ORR limiting current may not be broken down into R_{P} and R_{NP} due to the interference by the liquid water generated in the PtBS and diffusing through the PGM-free CL back to the flow fields. By comparing MEA1 and MEA4, which have approximately the same number of exchangeable protons in the CCL, the ORR limiting current results also suggest a higher gas transport resistance of the latter, explaining its lower PEMFC performance. Through the correlation between $R^{O_2}_{\text{total, 2×GDL}}$ and the current density in the mass transport limited region of the H_2/air polarization curves at 100% RH (e.g., at 0.2 V), it is very evident that MEA3, which has the highest R_{total}, delivered the smallest current density. This demonstrates that the proposed ORR limiting current method is useful to determine the mass transfer properties of PGM-free CCLs at 100% RH in air because it considers the effects of liquid water generation. Because only 5% O_2 was used during the limiting current experiments, the results were not correlated with the current density recorded in H_2/O_2, where pure O_2 reactants enable a sufficiently high diffusion coefficient.

The schemes of the PGM-free catalyst particles and the different EW of ionomers representing the HOR limiting current scenario and the ORR limiting current scenario are shown in Figure 9A,B, respectively. Without considering the water uptake, at a given I/C ratio, lower EW ionomer occupies less space in the CCL due to its shorter backbone and side chain, leading to a more porous electrode for H_2 molecules to diffuse through, as demonstrated by the pressure-independent gas transport resistance determined using HOR limiting current measurements. However, when the ORR occurred with a large amount of liquid water generated, at a given I/C ratio, the lower EW ionomer showed a higher number of exchangeable protons with more water molecules associated with a given volume of ionomer, causing more swelling. This leads to higher obstacles for O_2 to diffuse to the catalytic sites, as determined from the ORR limiting current measurement.

3 | CONCLUSIONS

Overall, the ionomer EW and the I/C ratio showed a great impact on the performance of PEMFCs with PGM-free cathodes, especially considering operation under different RH conditions. The results demonstrated that at a given I/C ratio, the ionomer with a lower EW (having a higher number of exchangeable protons) resulted in a less dense electrode structure, with smaller catalyst aggregate sizes, higher electrode capacitance, and a less tortuous H^+ transfer pathway. All these factors are critical in improving the electrode performance, especially in the kinetic-controlled region of the polarization curve (low current density). To explain the trend of the results observed in the diffusion-controlled region of the polarization curve (high current density), the gas transport resistance in the bulk electrode was measured using both a previously reported HOR limiting current method, and a newly developed ORR limiting current method. The pressure-independent gas transport resistance from the HOR experiments suggested that the ionomer with lower EW enabled better gas diffusivity within the CL. In comparison with the HOR counterpart, the ORR limiting current method used O_2 as a probe molecule, and the PGM-free catalyst did not participate

26924552, 2023, 1, Downloaded from https://onlinelibrary.wiley.com/doi/10.1002/sus2.106 by National Renewable Energy Lab, Wiley Online Library on [28/02/2023]. See the Terms and Conditions (https://onlinelibrary.wiley.com/terms-and-conditions) on Wiley Online Library for rules of use; OA articles are governed by the applicable Creative Commons License

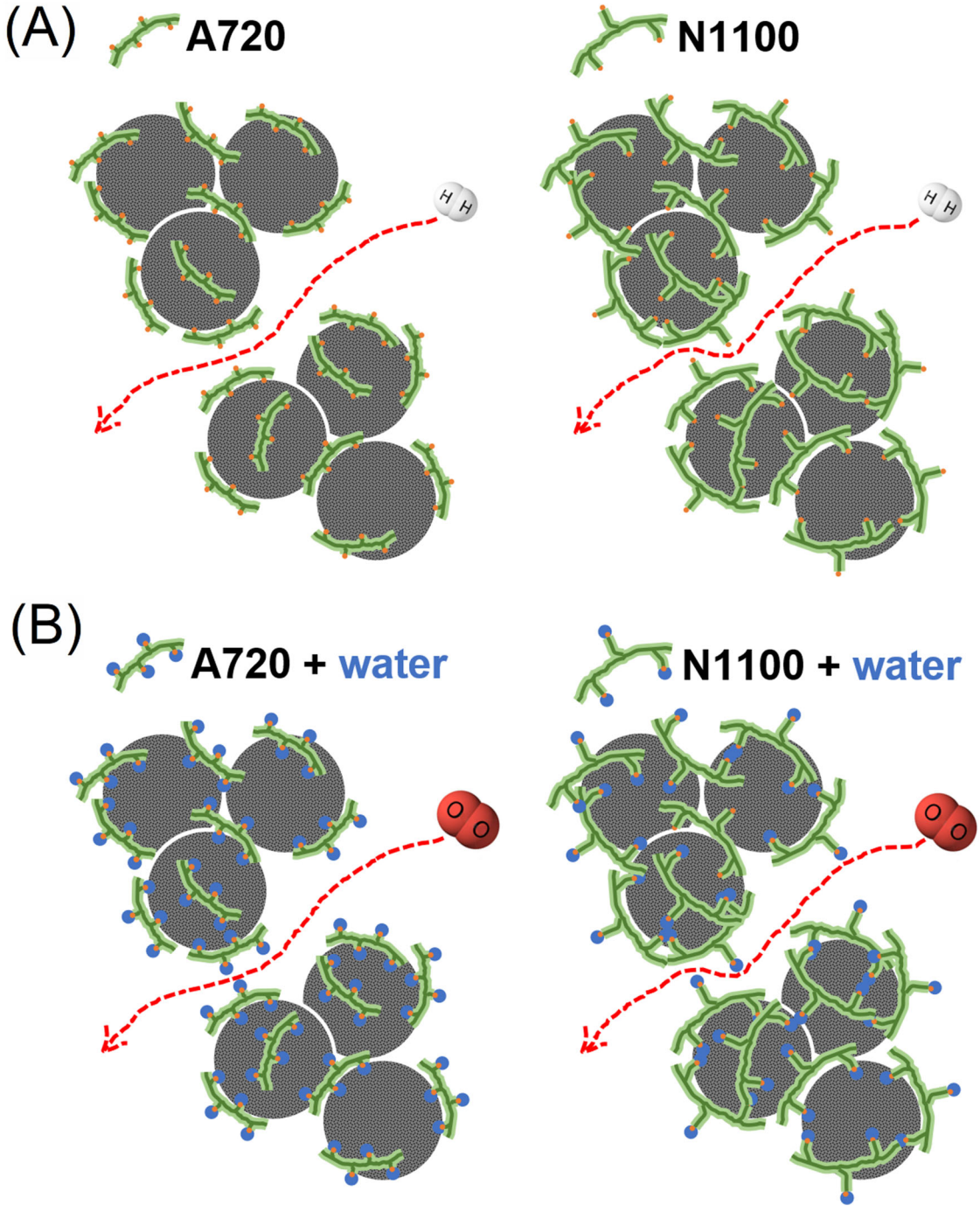

FIGURE 9 Scheme of the Pt group metal (PGM)-free catalyst aggregates and different equivalent weight (EW) of ionomer representing (A) the hydrogen oxidation reaction (HOR) limiting current testing scenario and (B) the oxygen reduction reaction (ORR) limiting current testing scenario

in the reaction but still interacted with the liquid water generated from PtBS, further affecting oxygen diffusion. The ORR limiting current results demonstrated that at a given I/C ratio, ionomers with lower EW showed increased obstacles for O_2 diffusion due to enhanced liquid water uptake, explaining the H_2/air and H_2/O_2 performance at high RH and at high current density. To the best of our knowledge, this new ORR limiting current tool has been used for the first time to study oxygen diffusion in the presence of liquid water for PGM-free electrodes. By better understanding the fundamental phenomena, this work may open up a new avenue to boost the performance of PEMFCs with PGM-free cathodes by leveraging the ionomer–catalyst interactions in the CL.

26924552, 2023, 1, Downloaded from https://onlinelibrary.wiley.com/doi/10.1002/sus2.106 by National Renewable Energy Lab, Wiley Online Library on [28/02/2023]. See the Terms and Conditions (https://onlinelibrary.wiley.com/terms-and-conditions) on Wiley Online Library for rules of use; OA articles are governed by the applicable Creative Commons License

4 | EXPERIMENTAL SECTIONS

4.1 | Materials

All materials were used without further purification. A Nafion N211 (DuPont, USA) membrane and a 29BC carbon paper GDL with a microporous layer (SGL Carbon) were used for all the MEAs. The water used in this work was high-purity Milli-Q water with a resistivity of 18.25 MΩ cm. *n*-Propanol (*n*PA) was purchased from Sigma-Aldrich, USA. A LIQUION LQ-1105 5 wt.% Nafion 1100 EW (N1100) dispersion was purchased from Ion Power Inc., and an Aquivion 720 EW (A720) 25 wt.% dispersion was purchased from Sigma-Aldrich. The 25 wt.% A720 dispersion was diluted into a 5 wt.% dispersion before use. The PGM-free Fe–N–C catalyst (PMF-011904) was purchased from Pajarito Powder LLC (USA).

4.2 | MEA fabrication and cell assembly

4.2.1 | Polarization curve measurement

The MEA fabrication was based on a modification of our previously reported procedure.[42,43] The cathode catalyst ink was prepared by dispersing 30 mg of Fe–N–C catalyst in a 5 wt.% ionomer dispersion and solvent mixture of water and *n*PA in various ratios, as reported in Table S1. The total volume of *n*PA and water was kept constant for all the inks. The resulting mixture was ultrasonicated for at least 2 h in an ice bath to generate a homogenous ink dispersion.

The anode gas diffusion electrode (GDE) was prepared, as described in previous reports, by ultrasonically spray coating a Pt/C catalyst (50 wt.% Pt on high surface area carbon catalyst TEC10E50E, TKK Corp., Japan) ink onto the GDL. The final Pt loading was determined to be 0.2 mg_{Pt} cm^{-2} by X-ray fluorescence spectroscopy using a Fischer FISCHERSCOPE X-RAY XDV-SDD instrument. The obtained anode GDE was further sprayed with an ionomer overlayer to minimize electrode/membrane contact resistance.[44] The anode GDE was hot-pressed onto the Nafion 211 membrane at 120°C and 4 MPa for 5 min to form a half-MEA.

The resulting half-MEA was placed onto a vacuum heating plate, which was set at 85°C, with the membrane side facing up. The Fe–N–C catalyst ink was deposited on the membrane using a paintbrush to achieve a catalyst loading of 4 mg cm^{-2} (Figure 1A).

All the MEAs were assembled in 5 cm^2 cell hardware, with a 14-parallel straight channel flow field[38] by placing a piece of SGL 29BC GDL on the cathode side without hot pressing. PTFE gaskets of 5 mil thickness were used on the anode side and 10 mil thickness on the cathode side. The hardware was tightened with a torque of 40 lb in.

4.2.2 | HOR limiting current measurement

The MEAs for HOR limiting current measurements were prepared in the same way as the aforementioned, except that a PtBs layer (prepared using Pt black catalyst TEC90300, TKK Corp., Japan) with a loading of ca. 0.7 mg_{Pt} cm^{-2} was deposited, by ultrasonic spray coating, on the cathode side of the MEA before the deposition of the PGM-free catalyst (Figure 8A).[30,41] The single-cell assembly for the HOR limiting current measurements was the same as that for the polarization curve measurements.

4.2.3 | ORR limiting current measurement

The MEA comprising anode GDE/membrane/PtBS was fabricated in the same way as described for the HOR limiting current measurements. The only difference was that the PGM-free catalyst ink was hand-painted onto a piece of SGL 29BC GDL instead of on the PtBs layer. During the painting, the SGL 29BC GDL was fixed onto a hot plate, which was set at 85°C.

For the ORR limiting current experiments, the cell was assembled by placing an additional piece of SGL 29BC GDL between PtBS and the PGM-free catalyst GDE, with the microporous layer of the GDL facing the membrane, to interrupt the H^+ transfer pathway from the membrane to the PGM-free CL. In this way, the ORR cannot occur within the PGM-free CL, but only on the PtBS.

4.3 | MEA testing

4.3.1 | Polarization curve measurement

After assembly, the cell was connected to a Hydrogenics fuel cell test station. Ultrahigh-purity gases (General Air, Commerce City, Colorado, USA) were used for all the tests. N_2 was fed to both electrodes while heating the cell to 80°C. The anode gas was then switched to H_2, and then the cathode gas was switched to air while monitoring the cell open-circuit voltage (OCV) until it reached a stable value. The polarization curves were measured with a cell temperature of 80°C and with different RH values of 50%, 75%, and 100%, adjusting the total cell pressure to have 100 kPa gas partial pressure (H_2 on anode, and air or O_2 on cathode). The gas flow rates were set to 1.0 L min^{-1} on both the anode and cathode for all the tests, to assure high stoichiometry, and hence differential cell conditions with the

26924552, 2023, 1, Downloaded from https://onlinelibrary.wiley.com/doi/10.1002/sus2.106 by National Renewable Energy Lab, Wiley Online Library on [28/02/2023]. See the Terms and Conditions (https://onlinelibrary.wiley.com/terms-and-conditions) on Wiley Online Library for rules of use; OA articles are governed by the applicable Creative Commons License

flow field used. The polarization curves were recorded in voltage control mode starting from the OCV, with a hold time of 75 s per point, and the current density was averaged for the last 60 s of the voltage hold. High-frequency resistance (HFR) was measured at 6000 Hz concurrently with polarization curve data acquisition.

After the polarization curves were recorded, cyclic voltammograms (CVs) of the cathode of the MEAs were measured under H_2/N_2 (anode/cathode gas flows at 100 ml min^{-1}) at 80°C and different RH values (25%, 50%, 75%, 90%, and 100%) between 0.0 and 1.0 V at 20 mV s^{-1}, adjusting the total cell pressure to keep the gas partial pressure to 100 kPa to avoid reference shifts due to the variation of H_2O partial pressure when varying the RH.

Electrochemical impedance spectroscopy (EIS) of the cathodes of the MEAs was measured under H_2/N_2 (anode/cathode gas flows at 100 ml min^{-1}) at 80°C and different RH values (25%, 50%, 75%, 90%, and 100%) in potentiostatic mode at 0.2 V, with a 3 mV AC amplitude, between 100 kHz and 0.1 Hz. The total cell pressure was adjusted when RH was changed as described previously. Both CV and EIS were measured with a Gamry potentiostat/galvanostat (Model Reference 3000).

4.3.2 | HOR limiting current measurement

The gas mass transport resistance in the cathode CL (CCL) in the absence of product water was determined using HOR limiting current measurements, as described in detail in our previous papers.[30,41]

Before the HOR limiting current measurements, the cell was conditioned using a Hydrogenics fuel cell test station, according to a protocol described elsewhere,[45] to fully activate the PtBS layer. After conditioning, the cell was connected to a Teledyne Medusa fuel cell test station, the cell temperature was set to 80°C, and 5% H_2 diluted by N_2 was fed on both electrodes with a flow rate of 2.0 L min^{-1} (anode) and 5.0 L min^{-1} (cathode). The HOR limiting current was measured using a Metrohm Autolab potentiostat (Model PGSTAT302N) recording CVs at 40 mV s^{-1} between 0.05 and 0.80 V, at different RH values of 50%, 75%, 90%, and 100%. At each RH value, CV was measured at four different cell pressures: 150, 200, 250, and 300 kPa. The HOR limiting current values were then used to extract the gas mass transport resistance, after subtracting the background CV measured when flowing N_2 on the cathode.

4.3.3 | ORR limiting current measurement

ORR limiting current measurements were performed to determine the gas mass transport resistance in the CCL in the presence of product water, which is generated by the ORR at the PtBS.

The PtBS was activated for the ORR by the fuel cell conditioning procedure, as described for the HOR limiting current experiments. After conditioning, the cell was heated to 80°C. Pure H_2 was fed to the anode, and 5% O_2 diluted by N_2 was fed to the cathode at flow rates of 1.0 and 5.0 L min^{-1}, respectively. The ORR limiting current data were measured using the same Metrohm Autolab potentiostat recording CVs at 40 mV s^{-1} between 0.10 and 1.10 V, at RH values of 50%, 75%, 90%, and 100%. At each RH value, CVs were measured at four different cell pressures: 150, 200, 250, and 300 kPa. The ORR limiting current values were then used to extract the gas mass transport resistance, after subtracting the background CV measured with N_2 on the cathode, as described in our previous works.[30,41]

4.4 | Material characterizations

4.4.1 | Electron microscopy measurements

Cross sections of the MEAs were prepared for STEM analysis by diamond knife ultramicrotomy. The distribution of the ionomer in the CL was quantified by X-ray energy-dispersive spectroscopy (EDS) on a Talos F200X ChemiSTEM (Thermo Fisher Scientific) operated at 200 kV. Elemental maps of fluorine were collected at low magnification (5k×) and high magnifications (20k×, 28k×, and 56k×). All maps were collected with an image size of 512 × 512 pixels at a beam current of 490 pA for 300 s. Elemental maps of fluorine were processed with in-house-made Python code to extract the distribution of the ionomer.

4.4.2 | Rheology measurements

Rheological measurements were performed, as reported in our previous studies,[46] on a stress-controlled rheometer (Thermo Scientific HAAKE MARS 60 Rheometer). Briefly, the measurements were performed using a stainless steel parallel-plate geometry (40 mm diameter) with a gap of 500 μm at 25°C. A solvent trap was used to prevent any solvent evaporation during the measurements. Prior to making measurements, the samples were preconditioned to erase any sample loading history on the microstructure by conducting a pre-shear at 500 s^{-1} for 1 min and then allowed to rest for 1 min. The steady-shear rheology measurements were performed by imposing a decreasing shear rate sweep in logarithmic steps ranging from 500 to 0.01 s^{-1} Pa. All the data reported were ensured to reach steady state. Amplitude measurements were also conducted to compare the viscoelasticity of the inks. The

26924552, 2023, 1, Downloaded from https://onlinelibrary.wiley.com/doi/10.1002/sus2.106 by National Renewable Energy Lab, Wiley Online Library on [28/02/2023]. See the Terms and Conditions (https://onlinelibrary.wiley.com/terms-and-conditions) on Wiley Online Library for rules of use; OA articles are governed by the applicable Creative Commons License

pre-shear protocol was similar to the steady-state rheology measurements. The frequency was fixed at 0.5 Hz, and the strain amplitude was increased logarithmically from 0.0001 to 10. To better capture the differences in the agglomerated structure, the inks used for the rheological measurements are slightly more concentrated inks (3.22 wt.% catalyst w.r.t. total ink) compared to the inks used to prepare MEA fabrication (2.53 wt.% catalyst). The inks were also dispersed/mixed differently using ball mill more suitable for concentrated inks, rather than by sonication. The mixing procedure is similar to our previous study,[43] where high-density zirconia beads (5 mm diameter, Glen Mills, Inc.) were used as a mixing media, and the inks were mixed for ~18 h at 80 rpm. These differences are not expected to significantly affect the inferences of the electrode structure based on ink microstructure.

4.4.3 | X-ray scattering

The catalyst structure in the electrode was characterized using X-ray scattering with a monochromatic X-ray beam in the range of 16.8–21 keV and a Q-range from 0.0001 to 6 $Å^{-1}$ at beamline 9ID-C, Advanced Photon Source (APS), Argonne National Laboratory (ANL). The ultrasmall-angle X-ray scattering (USAXS) and small-angle X-ray scattering (SAXS) data were collected with X-ray exposure times of 90 and 30 s, respectively. The X-ray intensity data were sequentially recorded in two scattering angle ranges of 10^{-4}–6×10^{-2} $Å^{-1}$ for the USAXS and 3×10^{-2}–1 $Å^{-1}$ for the pinhole SAXS. The CCL was removed from the membrane and transferred to Scotch tape. The background scattering data from Scotch tape were recorded and subtracted from the scattering data for each CCL sample. The scattering data were analyzed using the Irena data fitting macro package (Jan Ilavsky, APS, beamline 9ID-C) on the Igor Pro (WaveMetrics, OR) platform for data manipulations and simulations of scattering model functions.[47]

4.4.4 | Nano-CT

Following the procedure described in the work of Guetaz et al. and Komini Babu et al., sulfonic acid groups of the ionomer in the electrode samples were ion exchanged with Cs^+.[48,49] The electrode layers were sectioned into flakes to fit into the field of view (50 μm) and mounted on tomography needles. X-ray radiographs were acquired at 8 keV using the Xradia nanoXCT-S100 TXM at beamline 32-ID-C of the APS at ANL. With a 0.5 s exposure time, 1080 projection images were recorded over 180° of rotation and reconstructed into a 3D image sequence with a 20 nm voxel size as described in a previous work.[50] Data were acquired in both absorption and phase contrast modes. The phase contrast mode resolves the overall morphology of the secondary pores and the solid material (a mixture of catalyst, ionomer, and pores below resolution), whereas the absorption contrast images provide an intensity map of the high electron-density materials within the sample (i.e., Cs^+ in the ion-exchanged ionomer).

ACKNOWLEDGMENTS

This work was authored in part by Alliance for Sustainable Energy, LLC, the manager and operator of the National Renewable Energy Laboratory for the U.S. Department of Energy (DOE) under Contract No. DE-AC36-08GO28308. Argonne National Laboratory is managed for the U.S. Department of Energy by the University of Chicago Argonne, LLC, also under contract DE-AC-02-06CH11357. Research performed as part of the Electrocatalysis Consortium (ElectroCat), established as part of the Energy Materials Network, which is supported by the U.S. Department of Energy, Office of Energy Efficiency and Renewable Energy, Hydrogen and Fuel Cell Technologies Office (HFTO). This research used resources of the Advanced Photon Source (APS), a U.S. Department of Energy Office of Science User Facility operated for the DOE Office of Science by Argonne National Laboratory under Contract No. DE-AC02-06CH11357. The authors would like to thank the APS scientists: Vincent De Andrade at 32-ID-C and Jan Ilavsky and Ivan Kuzmenko at 9-ID-C. The authors wish to thank Dimitrios Papageorgopoulos and Simon Thompson in FCTO at DOE for supporting this work. While we do not endorse any materials presented in this study, we wish to thank Alexey Serov and Bar Zulevi of Pajarito Powders LLC for the use of their electrocatalyst. The views expressed in the article do not necessarily represent the views of the DOE or the U.S. Government.

CONFLICTS OF INTEREST

The authors declare no conflicts of interest.

ORCID

Luigi Osmieri https://orcid.org/0000-0002-3111-2270
Sunilkumar Khandavalli https://orcid.org/0000-0003-3179-5718

REFERENCES

1. Wang M, Medina S, Pfeilsticker JR, Pylypenko S, Ulsh M, Mauger SA. Impact of microporous layer roughness on gas-diffusion-electrode-based polymer electrolyte membrane fuel cell performance. *ACS Appl Energy Mater*. 2019;2(11):7757-7761.
2. Gottesfeld S, Zawodzinski TA. Polymer electrolyte fuel cells. *Adv Electrochem Sci Eng*. 2008:195-301.
3. Litster S, McLean G. PEM fuel cell electrodes. *J Power Sources*. 2004;130(1-2):61-76.

26924552, 2023, 1, Downloaded from https://onlinelibrary.wiley.com/doi/10.1002/sus2.106 by National Renewable Energy Lab, Wiley Online Library on [28/02/2023]. See the Terms and Conditions (https://onlinelibrary.wiley.com/terms-and-conditions) on Wiley Online Library for rules of use; OA articles are governed by the applicable Creative Commons License

4. Yoshida T, Kojima K. Toyota MIRAI fuel cell vehicle and progress toward a future hydrogen society. *Electrochem Soc Interface*. 2015;24(2):45-49.
5. Wang H, Kou RH, Jin Q, et al. Boosting the oxygen reduction performance via tuning the synergy between metal core and oxide shell of metal−organic frameworks-derived Co@CoOx. *ChemElectroChem*. 2020;7(7):1590-1597.
6. Wang H, Yin FX, Chen BH, et al. ZIF-67 incorporated with carbon derived from pomelo peels: A highly efficient bifunctional catalyst for oxygen reduction/evolution reactions. *Appl Catal B: Environ*. 2017;205:67.
7. Wang XX, Hwang S, Pan YT, et al. Ordered Pt3Co intermetallic nanoparticles derived from metal-organic frameworks for oxygen reduction. *Nano Lett*. 2018;18(7):4163-4171.
8. Banham D, Choi JY, Kishimoto T, Ye S. Integrating PGM-free catalysts into catalyst layers and proton exchange membrane fuel cell devices. *Adv Mater*. 2019;31(31):1804846.
9. Liu S, Li C, Zachman MJ, et al. Atomically dispersed iron sites with a nitrogen–carbon coating as highly active and durable oxygen reduction catalysts for fuel cells. *Nat Energy*. 2022;7(7):652-663.
10. Thompson ST, Papageorgopoulos D. Platinum group metal-free catalysts boost cost competitiveness of fuel cell vehicles. *Nat Catal*. 2019;2(7):558-561.
11. Pivovar B. Catalysts for fuel cell transportation and hydrogen related uses. *Nat Catal*. 2019;2(7):562-565.
12. Osmieri L. Transition metal–nitrogen–carbon (M–N–C) catalysts for oxygen reduction reaction. insights on synthesis and performance in polymer electrolyte fuel cells. *ChemEngineering*. 2019;3(1):16.
13. Jasinski R. A new fuel cell cathode catalyst. *Nature*. 1964;201:1212-1213.
14. Wang H, Grabstanowicz LR, Barkholtz HM, et al. Impacts of imidazolate ligand on performance of zeolitic-imidazolate framework-derived oxygen reduction catalysts. *ACS Energy Lett*. 2019;4(10):2500-2507.
15. Wang H, Yin FX, Liu N, et al. Engineering Fe–Fe3C@Fe–N–C active sites and hybrid structures from dual metal–organic frameworks for oxygen reduction reaction in H2–O2 fuel cell and Li–O2 battery. *Adv Funct Mater*. 2019;29(23):1901531.
16. Chung HT, Cullen DA, Higgins D, et al. Direct atomic-level insight into the active sites of a high-performance PGM-free ORR catalyst. *Science (80–)*. 2017;357(6350):479-484.
17. Wu G, More KL, Johnston CM, Zelenay P. High-performance electrocatalysts for oxygen reduction derived from polyaniline, iron, and cobalt. *Science (80–)*. 2011;332(6028):443-447.
18. Banham D, Kishimoto T, Zhou Y, et al. Critical advancements in achieving high power and stable nonprecious metal catalyst – based MEAs for real-world proton exchange membrane fuel cell applications. *Sci Adv*. 2018;4(3):eaar7180.
19. Akula S, Mooste M, Zulevi B, et al. Mesoporous textured Fe-N-C electrocatalysts as highly efficient cathodes for proton exchange membrane fuel cells. *J Power Sources*. 2022;520:230819.
20. Neyerlin KC, Gu W, Jorne J, Clark A, Gasteiger HA. Cathode catalyst utilization for the ORR in a PEMFC. *J Electrochem Soc*. 2007;154(2):B279-B287.
21. Gasteiger HA, Kocha SS, Sompalli B, Wagner FT. Activity benchmarks and requirements for Pt, Pt-alloy, and non-Pt oxygen reduction catalysts for PEMFCs. *Appl Catal B: Environ*. 2005;56(1-2):9-35.
22. Jaouen F, Jones D, Coutard N, Artero V, Strasser P, Kucernak A. Toward platinum group metal-free catalysts for hydrogen/air proton-exchange membrane fuel cells. *Johns Matthey Technol Rev*. 2018;62(2):231-255.
23. Lefèvre M, Proietti E, Jaouen F, Dodelet JP. Iron-based catalysts with improved oxygen reduction activity in polymer electrolyte fuel cells. *Science (80–)*. 2009;324(5923):71-74.
24. Mauger SA, Neyerlin KC, Yang-Neyerlin AC, More KL, Ulsh M. Gravure coating for roll-to-roll manufacturing of proton-exchange-membrane fuel cell catalyst layers. *J Electrochem Soc*. 2018;165(11):F1012-F1018.
25. Lo Vecchio C, Serov A, Romero H, et al. Commercial platinum group metal-free cathodic electrocatalysts for highly performed direct methanol fuel cell applications. *J Power Sources*. 2019;437.
26. Osmieri L, Wang H, Neyerlin KC. Impact of fabrication and testing parameters on the performance of a polymer electrolyte fuel cell with platinum group metal (PGM)-free cathode catalyst impact of fabrication and testing parameters on the performance of a polymer electrolyte fuel cell. *J Electrochem Soc*. 2021;168:014503.
27. Wang M, Park JH, Kabir S, et al. Impact of catalyst ink dispersing methodology on fuel cell performance using in-situ X-ray scattering. *ACS Appl Energy Mater*. 2019;2(9):6417-6427.
28. Van Cleve T, Khandavalli S, Chowdhury A, et al. Dictating Pt-based electrocatalyst performance in polymer electrolyte fuel cells, from formulation to application. *ACS Appl Mater Interfaces*. 2019;11(50):46953-46964.
29. Park J, Myers DJ. Novel platinum group metal-free catalyst ink deposition system for combinatorial polymer electrolyte fuel cell performance evaluation. *J Power Sources*. 2020;480:228801.
30. Wang G, Osmieri L, Star AG, Pfeilsticker J, Neyerlin KC. Elucidating the role of ionomer in the performance of platinum group metal-free catalyst layer via in situ electrochemical diagnostics. *J Electrochem Soc*. 2020;167(4):044519.
31. Yin X, Lin L, Chung HT, et al. Effects of MEA fabrication and ionomer composition on fuel cell performance of PGM-free ORR catalyst. *ECS Trans*. 2017;77(11):1273-1281.
32. Eisman GA. The application of Dow Chemical's perfluorinated membranes in proton-exchange membrane fuel cells. *J Power Sources*. 1990;29(3-4):389-398.
33. Kusoglu A, Dursch TJ, Weber AZ. Nanostructure/swelling relationships of bulk and thin-film pfsa ionomers. *Adv Funct Mater*. 2016;26(27):4961-4975.
34. Kusoglu A, Weber AZ. New insights into perfluorinated sulfonic-acid ionomers. *Chem Rev*. 2017;117(3):987-1104.
35. Lei C, Bessarabov D, Ye S, Xie Z, Holdcroft S, Navessin T. Low equivalent weight short-side-chain perfluorosulfonic acid ionomers in fuel cell cathode catalyst layers. *J Power Sources*. 2011;196(15):6168-6176.
36. Peron J, Edwards D, Haldane M, et al. Fuel cell catalyst layers containing short-side-chain perfluorosulfonic acid ionomers. *J Power Sources*. 2011;196(1):179-181.
37. Park YC, Kakinuma K, Uchida H, Watanabe M, Uchida M. Effects of short-side-chain perfluorosulfonic acid ionomers as binders on the performance of low Pt loading fuel cell cathodes. *J Power Sources*. 2015;275:384-391.

26924552, 2023, 1, Downloaded from https://onlinelibrary.wiley.com/doi/10.1002/sus2.106 by National Renewable Energy Lab, Wiley Online Library on [28/02/2023]. See the Terms and Conditions (https://onlinelibrary.wiley.com/terms-and-conditions) on Wiley Online Library for rules of use; OA articles are governed by the applicable Creative Commons License

38. Baker DR, Caulk DA, Neyerlin KC, Murphy MW. Measurement of oxygen transport resistance in PEM fuel cells by limiting current methods. *J Electrochem Soc*. 2009;156(9):B991-B1003.
39. Greszler TA, Caulk D, Sinha P. The impact of platinum loading on oxygen transport resistance. *J Electrochem Soc*. 2012;159(12):F831-F840.
40. Malevich D, Halliop E, Peppley BA, Pharoah JG, Karan K. Investigation of charge-transfer and mass-transport resistances in PEMFCs with microporous layer using electrochemical impedance spectroscopy. *J Electrochem Soc*. 2009;156(2):B216.
41. Star AG, Wang G, Medina S, Pylypenko S, Neyerlin KC. Mass transport characterization of platinum group metal-free polymer electrolyte fuel cell electrodes using a differential cell with an integrated electrochemical sensor. *J Power Sources*. 2020;450:227655.
42. Ahluwalia RK, Wang X, Osmieri L, Peng JK, Chung HT, Neyerlin KC. Performance of polymer electrolyte fuel cell electrodes with atomically dispersed (AD) Fe-C-N ORR catalyst. *J Electrochem Soc*. 2019;166(14):F1096-F1104.
43. Osmieri L, Wang G, Cetinbas FC, et al. Utilizing ink composition to tune bulk-electrode gas transport, performance, and operational robustness for a Fe–N–C catalyst in polymer electrolyte fuel cell. *Nano Energy*. 2020;75:104943.
44. Mauger SA, Pfeilsticker JR, Wang M, et al. Fabrication of high-performance gas-diffusion-electrode based membrane-electrode assemblies. *J Power Sources*. 2020;450:227581.
45. Kabir S, Myers DJ, Kariuki NN, et al. Elucidating the dynamic nature of fuel cell electrodes as a function of conditioning: an ex-situ materials characterization and in-situ electrochemical diagnostic study. *ACS Appl Mater Interfaces*. 2019;11(48):45016-45030.
46. Khandavalli S, Park JH, Kariuki NN, et al. Rheological investigation on the microstructure of fuel cell catalyst inks. *ACS Appl Mater Interfaces*. 2018;10(50):43610-43622.
47. Ilavsky J, Zhang F, Allen AJ, Levine LE, Jemian PR, Long GG. Ultra-small-angle X-ray scattering instrument at the advanced photon source: history, recent development, and current status. *Metall Mater Trans A*. 2013;44(1):68-76.
48. Guetaz L, Lopez-Haro M, Escribano S, et al. Catalyst-layer ionomer imaging of fuel cells. *ECS Meet Abstr*. 2015;MA2015-02(37):1471-1471.
49. Komini Babu S, Chung HT, Zelenay P, Litster S. Resolving electrode morphology's impact on platinum group metal-free cathode performance using nano-CT of 3D hierarchical pore and ionomer distribution. *ACS Appl Mater Interfaces*. 2016;8(48):32764-32777.
50. Cetinbas FC, Ahluwalia RK, Kariuki N, et al. Hybrid approach combining multiple characterization techniques and simulations for microstructural analysis of proton exchange membrane fuel cell electrodes. *J Power Sources*. 2017;344:62-73.
51. Zhang J, Tang Y, Song C, et al. PEM fuel cell relative humidity (RH) and its effect on performance at high temperatures. *Electrochim Acta*. 2008;53(16):5315-5321.
52. Garsany Y, Atkinson RW, Sassin MB, Hjelm RME, Gould BD, Swider-Lyons KE. Improving PEMFC performance using short-side-chain low-equivalent-weight PFSA ionomer in the cathode catalyst layer. *J Electrochem Soc*. 2018;165(5):F381-F391.
53. Osmieri L, Ahluwalia RK, Wang X, et al. Elucidation of PGM-free electrocatalyst active site functionality via in-situ X-ray absorption and operando determination of oxygen reduction reaction kinetics in a PEFC. *Appl Catal B: Environ*. 2019;257:117929.
54. Li J, Alsudairi A, Ma ZF, Mukerjee S, Jia Q. Asymmetric volcano trend in oxygen reduction activity of Pt and non-Pt catalysts: in situ identification of the site-blocking effect. *J Am Chem Soc*. 2017;139(4):1384-1387.
55. Setzler BP, Fuller TF. A physics-based impedance model of proton exchange membrane fuel cells exhibiting low-frequency inductive loops. *J Electrochem Soc*. 2015;162(6):F519-F530.
56. Open Source Impedance Fitter (OSIF). https://github.com/NREL/OSIF
57. Diard JP, Le GorrecB, Montella C. Handbook of Electrochemical Impedance Spectroscopy – Diffusion Impedances. 2012.
58. Kabir S, Medina S, Wang G, Bender G, Pylypenko S, Neyerlin KC. Improving the bulk gas transport of Fe-N-C platinum group metal-free nanofiber electrodes via electrospinning for fuel cell applications. *Nano Energy*. 2020;73(March):104791.

SUPPORTING INFORMATION

Additional supporting information can be found online in the Supporting Information section at the end of this article.

How to cite this article: Wang H, Osmieri L, Yu H, et al. Elucidating the impact of the ionomer equivalent weight on a platinum group metal-free PEMFC cathode via oxygen limiting current. *SusMat*. 2023;3:72–90. https://doi.org/10.1002/sus2.106

26924552, 2023, 1, Downloaded from https://onlinelibrary.wiley.com/doi/10.1002/sus2.106 by National Renewable Energy Lab, Wiley Online Library on [28/02/2023]. See the Terms and Conditions (https://onlinelibrary.wiley.com/terms-and-conditions) on Wiley Online Library for rules of use; OA articles are governed by the applicable Creative Commons License